This is a repository copy of *Pore-scale dynamics of nanofluid-enhanced NAPL displacement in carbonate rock*.

White Rose Research Online URL for this paper:
https://eprints.whiterose.ac.uk/155922/

Version: Accepted Version

Article:

Qin, T, Goual, L, Piri, M et al. (2 more authors) (2020) Pore-scale dynamics of nanofluid-enhanced NAPL displacement in carbonate rock. Journal of Contaminant Hydrology, 230. 103598. ISSN 0169-7722

https://doi.org/10.1016/j.jconhyd.2019.103598

© 2019 Elsevier B.V. Licensed under the Creative Commons Attribution-NonCommercial-NoDerivatives 4.0 International License (http://creativecommons.org/licenses/by-nc-nd/4.0/).

Reuse

This article is distributed under the terms of the Creative Commons Attribution-NonCommercial-NoDerivs (CC BY-NC-ND) licence. This licence only allows you to download this work and share it with others as long as you credit the authors, but you can't change the article in any way or use it commercially. More information and the full terms of the licence here: https://creativecommons.org/licenses/

Takedown

If you consider content in White Rose Research Online to be in breach of UK law, please notify us by emailing eprints@whiterose.ac.uk including the URL of the record and the reason for the withdrawal request.

eprints@whiterose.ac.uk
https://eprints.whiterose.ac.uk/

Pore-scale Dynamics of Nanofluid-Enhanced NAPL Displacement in Carbonate Rock

Tianzhu Qin,[1] Lamia Goual,[1]* Mohammad Piri,[1] Zhongliang Hu,[2] Dongsheng Wen[2]

1. Department of Petroleum Engineering, University of Wyoming, Laramie, WY 82071, USA

2. Department of Chemical and Process Engineering, University of Leeds, Leeds, LS2 9JT, UK

* Email: lgoual@uwyo.edu, phone: 307-766-3278

ABSTRACT

This study consists of a pore-scale investigation of two-phase flow dynamics during nanofluid flooding in subsurface formations containing non-aqueous phase liquids (NAPLs) such as crude oils. The goal was to gain fundamental understanding of the dominant displacement mechanisms of NAPL at different stages of nanofluid injection in a carbonate rock using x-ray microtomography integrated with a miniature core-flooding system. The nanofluid consisted of surfactant-based microemulsions with *in-situ* synthesized silica nanoparticles. After establishing its initial wettability state, the carbonate core sample was subjected to various pore volumes (PV) of nanofluid flooding (from 0.5 to 10) to examine the impact on NAPL flow dynamics. We found that most NAPL mobilization occurred within the first PV of injection, removing nearly 50% of NAPL from the rock. The nanofluid invaded into larger pores first with piston-like displacement due to a sharp decrease in NAPL/brine interfacial tension (from 14 to 0.5 mN/m) and contact angle (from 140 to 88°). With higher amount of nanofluid delivered into the pores through advection and diffusion, over 90% of NAPL droplets were emulsified and their size decreased from 9 to 3 μm. Subsequent nanofluid injection could further remove NAPL from the smaller pores by altering the thickness of NAPL layers adsorbed on the rock. This dynamic solubilization process reached equilibrium after 5 PV of injection, leading to a reduced layer thickness (from 12 to 0.2 μm), a narrower *in-situ* contact angle distribution around 81°, and an additional 16% of NAPL removal.

Keywords: Pore-scale dynamics, Microemulsion, Crude oil, Nanoparticle, Enhanced oil recovery, Aquifer remediation.

1 INTRODUCTION

The displacement of non-aqueous phase liquids (NAPLs) such as crude oils by other immiscible fluids is important in many porous media applications, including groundwater remediation and oil recovery. The introduction of selective chemicals into injected brine can further promote the mobilization and solubilization of NAPL by reducing the threshold capillary pressure.[1–5] While these phenomena have been well documented under steady-state conditions, dynamic effects occurring at early stages of injection are still unclear. Microfluidics, confocal microscopy, and advanced imaging techniques such as x-ray microcomputed tomography (micro-CT) have been used in the past to gain fundamental understanding of the pore-scale dynamics of NAPL displacement in porous media.[2,6,7] Compared to indirect core-scale measurements, where material balance is often used to calculate NAPL recovery over time, these direct imaging techniques make it possible to visualize fluid occupancy in artificial glass specimens or natural rocks. Furthermore, these techniques can provide necessary links to fundamental pore-scale displacement processes, which cannot be observed by traditional core-scale measurements.[8–10] For example, a fast synchrotron x-ray CT scanner coupled with a miniature core-flooding system was used to examine the dynamics of NAPL mobilization by water flooding in a water-wet Berea sandstone. The brine phase could mobilize the trapped non-wetting phase by establishing dynamic fluid connectivity during steady-state flow, where the isolated non-wetting phase could be periodically reconnected and form temporary flow channels.[11] In oil-wet porous media, the brine (nonwetting phase) needed to overcome the negative threshold capillary pressure to mobilize NAPL inside the pores. During this drainage process, the nonwetting phase could fill dozens of pores in a single step, typically 10-20 pores per event. This phenomenon, known as Haines jumps, was attributed to a sharp increase in the non-wetting phase saturation when the burst occurred in the porous medium.[7,12]

Surfactant flooding has seen several applications in the petroleum and environmental industries. In this technique, a surfactant solution is injected into a well, flows through NAPL-bearing geologic formations, and is produced from another extraction point.[13] In the mobilization mechanism, surfactants tend to concentrate at NAPL/brine interfaces and reduce the interfacial tension (IFT), making it energetically favorable to remove NAPL from smaller pores compared to brine alone.[14] In the solubilization mechanism, as the surfactant concentration approaches its critical micelle concentration (CMC), molecules start to associate with each other to form micelles with a hydrophobic core. While these micelles dissociate and reform, they are able to incorporate NAPL into their core and carry them through the brine phase. The solubilization of adsorbed NAPL layers on the mineral surfaces can lead to the reversal of rock wettability from oil-wet towards neutral- or water-wet.[1–3,15,16]

Dynamic flow studies showed that surfactant molecules are in fact transported through porous media by advection and diffusion.[10] Their concentration gradients in a sandstone persisted over several millimeter length for several minutes during the flooding.[17] Upon injection, surfactant molecules could spontaneously emulsify NAPL inside the pores at low flow rates.[6,8] They also promoted the *in-situ* solubilization of NAPL in the rock. At early stages of alkali surfactant (AS) flooding, AS could mobilize a large fraction of NAPL (about 75%) and left isolated small NAPL clusters in single pores. These small clusters were gradually solubilized during the flooding and contributed to 25% of NAPL recovery. The remaining NAPL clusters after AS flooding were immobile due to capillary trapping and would only be removed after further solubilization.[9] To better understand the pore-scale dynamic mobilization and solubilization, direct pore-scale reactive transport modeling was performed with a carbonate rock and a surfactant. The simulations revealed that the dynamic wettability alteration of pore surfaces could cause a decrease in the amount of residual NAPL left in the invaded pore space and an increase in the number of pores that were invaded. This dynamic wettability alteration changed the number of pores and throats that became accessible to the invading brine during low salinity water flooding.[18]

The mobilization and solubilization capacity of surfactants in carbonates can be further enhanced by putting them into microemulsified state.[2–4] Microemulsions (MEs) are thermodynamically stable, isotropic, and macroscopically homogeneous dispersions of hydrocarbon and brine, often stabilized by a surfactant and co-surfactant.[19,20] The stability of MEs in harsh environments such as elevated temperatures and brine salinities can be boosted with the addition of few nanometer-sized nanoparticles (NPs).[21] Together, NPs and surfactants tend to adsorb at NAPL/brine interfaces to form stable pickering emulsions. The steric forces created by these complex nanofluids provide a mechanical barrier against coalescence and thermal fluctuations, such as lamella drainage and hole formation.[22–25] The ability of these nanofluids to mobilize and solubilize NAPL has been investigated using core-scale experimental techniques.[26–29] Soil core data indicated that approximately 70% of the prevalent NAPL was removed.[30] Hu and co-workers proposed a novel method to synthesize NPs inside MEs where a terpene solvent (such as limonene) was used as a carrier fluid. Synergistic interactions between NPs and surfactant molecules enhanced their adsorption at the limonene/water interface and made them less prone to aggregation or adsorption on the rock. Moreover, the ME stabilized by *in-situ* synthesized NP (or MENP) increased brine viscosity and NAPL displacement efficiency with an additional recovery of 19% compared to ME alone.[4]

The goal of this study was to gain fundamental understanding of the pore-scale dynamics of NAPL flow in carbonates and identify the dominant displacement mechanisms at different stages of MENP injection (i.e., 0.5-10 PVs). A micro-CT scanner integrated with a miniature core-flooding system was utilized to conduct these experiments at elevated pressure and temperature. Novel insights were gained on the pore-scale dynamics of spontaneous emulsification and solubilization of NAPL by MENP nanofluid.

2 EXPERIMENTAL MATERIALS AND METHODS

2.1 Materials

2.1.1 Rock

The rock consisted of an outcrop from Fond Du Lac carbonate formation in Wisconsin. A mother core with a diameter of 1.5 inches and length of 2 inches was drilled from the Fond Du Lac block and then dried at 110 ^{o}C for 24 hours. After cooling down to ambient temperature, the porosity and permeability of the core were measured using a Helium porosimeter-permeameter apparatus (AP -608, Coretest system), which were 14.5% and 137 mD, respectively. One miniature core sample with 5 mm in diameter and 48 mm in length was extracted from the mother core to be used in the miniature core-flooding experiments. The absolute brine permeability of the miniature core was measured to be 32 mD. The average tomography-based porosity was measured using the histogram threshold method and calculated to be 14.7%.

2.1.2 Fluids

We used a light crude oil from the Permian Basin in Texas as the NAPL phase. The oil was centrifuged at 6,000 rpm for one hour and then filtered through a 0.5 µm filter to remove any solid contaminants. The brine was synthesized based on the ionic concentration of the reservoir brine from the Permian basin (see **Table S1**). About 7 wt% of diiodomethane (>99%, Sigma Aldrich) was added to the oil to enhance the contrast between NAPL and brine phases in the microtomographic images.

2.2 Methods

2.2.1 Nanofluid preparation

We used Triton X-100 (laboratory grade, Sigma Aldrich) and n-dodecyl β- D-maltoside (>98%, Sigma Aldrich) as the nonionic surfactants and 2-propanol (ACS grade, Fisher Scientific) as the co-surfactant to stabilize d-limonene (96.9%, MP Biomedicals) in brine. The Triton/maltoside/d-limonene/2-propanol were mixed with a weight ratio of 2:2:1:0.8. Afterward, brine was added to the mixture in two steps: 1) until the water content is 15 wt%, stirred at 200 rpm for 10 min, 2) until brine content is 99.5%, stirred at 500 rpm for 10 min. The ME was transparent with a surfactant concentration of 0.33 wt%. The detailed preparation procedures are provided in previous studies.[2,3,31]

Tetraethyl orthosilicate (>99%, Sigma Aldrich) was selected as the oil-soluble precursor in order to synthesize silica (SiO_2) NPs *in-situ* in microemulsions. The precursor was first dissolved in d-limonene then the hydrocarbon mixture was used as a nanoreactor to control the sol-gel reaction between water and tetraethyl orthosilicate.[32] After contacting with water, tetraethyl orthosilicate formed silanol groups by hydrolysis and subsequently developed siloxane bridges by a condensation reaction, which resulted in the formation of single monodisperse SiO_2 nanoparticles, as shown in **Equation 1**.[32–35]

$$\mathrm{Si(OC_2H_5)_4 + 2H_2O \rightarrow SiO_2\downarrow + 4C_2H_6O} \tag{1}$$

The volume of tetraethyl orthosilicate was pre-determined so that the final concentration of NPs in ME was 0.01 wt%. To expedite the chemical reaction, NaOH solution (>97.0%, Fisher Scientific) was slowly added as a catalyst and mixed by an ultrasound probe with an amplitude of 25 until the solution pH reached 10. After reacting for seven days at 60 °C, the solution was titrated by diluted HCl (36.5-38.0%, Fisher Scientific) until the pH decreased to 7. Various salts were then added into the solution until the ion concentrations reached the values in **Table S1**.

2.2.3 Nanofluid characterization and thermal stability

An Environmental Transmission Electron Microscope (Titan ETEM G2, FEI) was used to visualize the morphology of ME and MENP at 220 kV. The nanofluids were carefully transferred onto PELCO silicon dioxide-support films (Ted Pella, Inc.) and dried overnight at ambient conditions before imaging. We used ImageJ software to analyze the micrographs and the nanofluid size distributions were measured based on over 100 different droplets. The thermal stability of nanofluids was also investigated using a sedimentation method by placing them in closed bottles at 25°C, 60°C, and 80 °C. After seven days, the solutions were examined to evaluate their sedimentation or phase separation behavior.

2.2.4 Dynamic interfacial tension and droplet size distribution

Dynamic interfacial tensions between NAPL and brine were measured with and without MENP using rising/captive bubble tensiometry enhanced by image acquisition with a high-resolution charge-coupled device (CCD) digital camera and apochromatically corrected lens. The experimental set up includes a Hastelloy measurement cell, a Hastelloy dual-cylinder pulse-free Quizix pump (to provide constant flow rate and pressure), a temperature control module, a data acquisition computer, an oven, and an in-line density meter (Anton Paar DMA HPM) to measure the density of fluids at actual experimental conditions. Injection needles with diameters between 0.711 and 1.762 mm were selected for IFT measurements to ensure that the Bond numbers were close to unity. The images were captured every 1 min and analyzed by the Axisymmetric Drop Shape Analysis (ADSA) software. More details of the experimental procedure can be found elsewhere.[36]

To evaluate the emulsification ability of the nanofluid, NAPL and brine solutions (50/50 vol.) were rigorously mixed for 5 h at a speed of 500 rpm. The rag layer between these two phases was diluted 20 times by the same brine to improve its transparency to light. The droplet size distribution of emulsions in the rag layer was visualized by an inverted microscope (IX83, Olympus) and analyzed by ImageJ software. More than 50 different droplets were evaluated in this analysis. The experimental procedure was repeated three times to estimate the experimental errors and average values were used in the droplet size distribution curves.

2.2.5 Rock characterization

We used Quantitative Evaluation of Minerals by Scanning Electron Microscopy (QEMSCAN 650F, FEI) to evaluate the mineralogy of Fond Du Lac carbonate. The x-ray source was optimized at 25 kV and 6.2 nA and a Species Identification Protocol “HMS Primary v 1.0" was used to convert raw data to 3 × 3 mm mineralogy maps with an optical resolution of 0.73 μm per pixel. The percentages of different minerals were further analyzed quantitatively and presented in **Table S2**. The pore size distribution of Fond Du Lac carbonate was also evaluated using a micro-CT scanner (VERSA-XRM500, Zeiss) with a resolution of 1.9 μm per pixel. The x-ray source was operated at a voltage of 90 kV and a power of 6 W. After acquiring the microtomographic images of the sample, the raw data were analyzed using Avizo Fire 9.4 software.

2.2.6 Flooding experiments

Microscale flow tests were performed with a miniature core flooding system integrated with a high-resolution x-ray micro-CT scanner (VERSA-XRM500, Zeiss). A schematic diagram of the experimental setup is displayed in **Figure S1 (a)**. The flow system consists of three programmable pulse-free, dual-cylinder 5000 Series Quizix pumps (one for back pressure regulation and two for NAPL and brine injection from the bottom of the core), three Rosemount differential pressure transducers, a custom-built miniature core holder made of carbon fiber, and flexible PFA tubings. The produced liquids were received from the top of the core at a constant back pressure. The middle section of the core (cylindrical field of view with 4 mm in diameter and 4 mm in length) was scanned at a resolution of 2.09 μm during the flooding tests. A voltage of 70 kV and a power of 6 W were employed to reduce the noise and enhance the quality of the micro-tomographic images.

In order to examine the dynamics of pore-scale displacement, one miniature Fond Du Lac core was flooded by various PVs of MENP nanofluid using the experimental procedure shown in **Figure S1 (b)**. The core was first placed in a miniature core holder with a confining pressure of 300 psi. Reference images were generated by scanning the middle section of the core at a resolution of 2.09 μm per voxel. After injecting

CO_2 into the flow system for one hour to remove any trapped air, the tubings and the core were vacuumed for 24 hours, saturated with brine, then flooded with several PVs of brine at 200 psi to dissolve all the trapped CO_2. NAPL was subsequently injected at a flow rate of 0.01 cc/min to establish the initial water saturation (S_{wi}). After aging the core dynamically with NAPL for fourteen days at 0.0002cc/min flow rate and 60 ^{o}C, various PVs of MENP were injected (0.5, 1, 2, 5, 8, 10) at a flow rate of 0.002 cc/min. In all flow tests, the back pressure and confining pressure were maintained at 200 psi and 400 psi, respectively. The same location of interest was scanned at the end of each flooding (i.e., primary drainage and nanofluid floodings).

2.2.7 Data acquisition and image analysis

Fluid occupancy maps obtained from the micro-CT images were used to investigate the pore-scale displacement physics that controls fluid flow inside the core. The tomography files obtained from the micro-CT were then re-constructed to obtain pore and fluid occupancy maps using Avizo Fire 9.4 software. During data processing, the non-local means filter was initially applied to smoothen the raw data and reduce noises.[37] Reference images of the dry core sample were segmented into pore maps, which presented the pore topology of Fond Du Lac carbonate. Each wet image set acquired after primary drainage and MENP flooding was manually registered to the reference image set pixel-by-pixel. To reduce errors caused by the close intensity of doped brine and eliminate grains from the flooded images, registered image sets were multiplied by the pore map of the reference image set. The wet image sets were segmented into the brine and NAPL phases to obtain fluid occupancy maps by applying the histogram threshold method.[38] The fluid occupancy maps were then used directly to measure the thickness of adsorbed oil layers and *in-situ* contact angles as shown in **Figure S2**. For each flooding test, *in-situ* contact angles were evaluated using over thirty NAPL droplets at different locations of the core with a maximum error of 9%. The selected droplets were examined in ten consecutive slides to identify the NAPL/brine/mineral contact line. The adsorbed NAPL layer thicknesses were measured over twenty locations in the core after each flooding test. Slice-averaged and total saturations of NAPL and brine were determined at the end of each flow test employing statistical analysis methods.

3 RESULTS

3.1 Rock characterization

Fond Du Lac carbonate is a homogeneous rock with respect to mineralogy and consists of 99.6% of dolomite with a small fraction of other minerals, as shown in **Figure 1** and **Table S2**. Its pore topology and size distribution were obtained from microtomography images and are displayed in the same figure. This rock has a wide pore size distribution with two peaks at about 15 µm and 110 µm, which indicates the presence of narrow throats and relatively larger pores. This characteristic makes it easier for the rock to trap NAPL. To determine whether the scanned field of view (FOV) was within porosity- and saturation-based representative elementary volume (REV), the variation of porosity and water saturation after injection 10 PV of MENP with changes in volume was investigated in **Figure S3**. The porosities and water saturation of cubical sub-volumes of the FOV with various lengths from 0.1 to 2.3 mm were calculated. The sub-volume beyond which the petrophysical properties showed no significant fluctuation was considered as the REV. **Figure S3** shows that the porosity and water saturation varied significantly until the cubical sub-volume lengths were large than 1.8 mm and 2.0 mm, respectively. These sub-volume lengths were much smaller than the length of the FOV (4 mm). Thus, the porosity and saturation estimated within the FOV can represent the overall properties of the core sample.

3.2 Microemulsion phase behavior

Figure S4 illustrates the preparation history and phase behavior of microemulsions from their pseudo-ternary phase diagram. Triton X-100, n-dodecyl β-D-maltoside, and 2-propanol were mixed at a fixed weight ratio of 2/2/0.8 to form Smix. D-limonene was then added to the solution at different weight ratios (from 1/9 to 9/1) and the phase diagram was obtained by titrating these mixtures with brine at different concentrations (from 10% to 90%). The dashed arrow depicted in **Figure S4** indicates the path of microemulsion dilution in brine until 0.33 wt% surfactant concentration was reached. When mixed at a specific weight ratio of 2/2/1/1/0.8, triton/maltoside/limonene/brine provided stable and transparent microemulsions at ambient conditions over a period of 6 months.[3] The S_{mix} to d-limonene ratio played an important role in the preparation of microemulsions. **Figure S4** shows that transparent microemulsions were formed in the area above the red dashed line during the titration process, where the ratio was higher than 3/7. In contrast, milky white emulsions were formed in the area below the red dashed line, where the ratio was lower than 3/7.

3.3. TEM micrographs and thermal stability

The TEM micrographs of ME, NP, and MENP are given in **Figure 2**, together with their size distributions. In MENP, a large number of small NPs with an average diameter of 2.7 nm were produced *in-situ* by the sol-gel reaction between water and tetraethyl orthosilicate.[4] These NPs remained at the d-limonene/water interface owing to the high detachment energy, and generated stable pickering emulsions.[4] As a result, the size of MENP droplets was slightly smaller than ME ones, with an average value of 65 nm compared to 79 nm. The stability of nanofluids was also examined at various temperatures using the sedimentation method in Section 2.1.3 (**Figure S5**). Both ME and MENP were stable and transparent at 25 ^{o}C and 60 ^{o}C for seven days, however ME became cloudy at 80 ^{o}C following the coalescence of d-limonene droplets. MENP, on the other hand, remained stable and transparent due to the presence of NPs, which provided an additional steric barrier toward coalescence. Therefore, MENP was selected as the chemical of choice in the following sections.

3.4 Dynamic interfacial tension and drop size distribution

The effect of MENP on the dynamic IFT between NAPL and brine was measured at 60 °C and 200 psi (**Figure 3**). The introduction of MENP to brine rapidly decreased the IFT from 14.2 to 0.49 mN/m due to the cumulative effect of surface-active additives (i.e., surfactants and nanoparticles) and organic solvents (i.e., carrier fluid and alcohol), which adsorbed at the NAPL/water interface or partitioned between the two phases, reduced the surface energy, and modified the polarity of NAPL and brine.[39] Synergistic effects between surfactants and NPs further enhanced the stability of the interfacial layer. Together, they exhibited a faster diffusion rate to the interface and a lower adsorption energy barrier (activation energy), resulting in faster IFT reduction with lower equilibrium values.[40]

The emulsification ability of MENP was quantitatively evaluated in **Figure 4** by analyzing the size of NAPL droplets in the diluted rug layer, according the procedures described in **Section 2.2.3**. In the synthesized reservoir bine, NAPL droplets had a bimodal distribution with two peaks at about 140 μm and 450 μm, respectively. The addition of MENP to brine reduced their size by over one order of magnitude (20 μm) and made them less polydisperse. This improved emulsification ability had significant implications of NAPL mobilization in the pore spaces, as presented in **Section 3.7**.

3.5 In-situ contact angle

The in-situ contact angles of NAPL droplets in the carbonate rock were measured at the end of primary drainage. **Figure 5** reveals that these angles spanned over a relatively wide range (i.e., from 90° to 180°) with an average value of 140 °. A large fraction of the pores became strongly NAPL-wet after the NAPL aging process and a smaller fraction was neutral-wet or weakly NAPL-wet. This wettability alteration could be explained by the formation of strong chemical bonds between carbonate and carboxylate groups of NAPL molecules, leading to the formation of adsorbed NAPL layers on the mineral surfaces.[2,9]

The dynamics of wettability reversal by MENP was investigated next. After injecting 0.5 and 1 PV of nanofluid, the average contact angle sharply reduced to 104° and 88°, respectively. The angle smaller than 90° indicates that threshold capillary pressures in the porous medium became positive, which favored NAPL mobilization through the rock. Injecting 2, 5, and 10 PV of MENP could further decrease the average contact angle to stabilize at 81°. Even though this decrease was not significant, it had a prominent impact on the angle distribution in the porous medium. **Figure 5** shows that the contact angles on carbonate surfaces had a wide distribution after 0.5 and 1 PV of nanofluid injection. With the limited amount of chemical delivered into the rock, MENP could not fully solubilize the adsorbed NAPL layers and a fraction of the pores remained NAPL-wet. After 2, 5 and 10 PV of nanofluid injection, these NAPL-wet pore surfaces were restored back to neutral or water-wet and exhibited a narrower contact angle distribution. This phenomenon was attributed to a higher solubilization of adsorbed NAPL layers by MENP, as discussed in the next sections.

3.6 Primary drainage

NAPL was injected at 0.01 cc/min into a core sample fully saturated with brine until an average initial water saturation of 10.7% was established. **Figure 6** displays the water saturation profile and its average value calculated from about 2000 slides in the FOV. Since the drainage was under capillary-dominated flow regime with a capillary number of about 1.6×10^{-6}, NAPL first invaded into the large pores and then gradually filled the smaller capillary elements (i.e., small pores and throats). This displacement pattern was confirmed in the two-dimensional images of pore spaces at the end of primary drainage (**Figure 7**).

3.7 MENP flooding

In order to examine the dynamics of NAPL removal by nanofluid flooding, different pore volumes of MENP (0.5, 1, 2, 5, and 10) were injected into the core at a flow rate of 0.002 cc/min. **Figure 6** presents the water saturation profiles after the injection of each PV. A significant increase in water saturation (from 10.7% to 49.3%) was observed during the first PV injected. The sharp IFT decline to 0.49 mN/m resulted in the formation of very small NAPL droplets that could be easily mobilized through the porous rock (**Figure 3**). MENP could also to restore the wettability of dolomite surfaces back to their water-wet state with an average contact angle of 88^o after 1 PV of MENP injection (**Figure 5**). As a result, the threshold capillary pressures were reduced by several orders of magnitude, enabling MENP to invade more pore/throat junctions and smaller pores, and consequently recover more NAPL.[41]

The superior ability of MENP to emulsify NAPL was confirmed by the direct pore-scale observations of NAPL displacement in **Figure 7.** A closer examination of the dynamic flooding process shows that the aqueous phase could spontaneously emulsify NAPL into small droplets after 0.5 PV of MENP injection. These smaller droplet sizes provided larger interfacial surface areas where NPs and surfactants interacted to form rigid layers that constituted mechanical barriers against coalescence.[22–25] Upon the injection of an additional 0.5 PV of MENP, most of the emulsified NAPL droplets were removed from the core. The spontaneous emulsification behavior was quantitatively analyzed using the statistical analysis module in Avizo. After selecting thirty pore spaces containing emulsified NAPL droplets, we found that MENP was able to mobilize 97.6% of these emulsions and reduce their average size from 9.4 µm to 3.1 µm after 1 PV of injection, as shown in **Figure 8.** With increasing amount of nanofluid injection, the dynamic process reached equilibrium and formed small emulsified NAPL droplets with 2.6 µm in diameter. This behavior could be explained by the dynamics of advection, diffusion, and adsorption of chemical additives in porous media.[10,42] During MENP injection, a fraction of additives adsorbed at the brine/NAPL and brine/rock interfaces and another fraction was diluted by the reservoir brine. Therefore, the additive concentrations inside the core were lower than those prior to injection. With larger amount of MENP delivered into the pores, the concentration of MENP gradually increased and reached equilibrium.

The solubilization ability of MENP was investigated by examining the layer thinning process at the angle of view shown in **Figure 7 (a)**. To better visualize the adsorbed NAPL layers, the fluid configuration in the capillary element was presented in three-dimensions without the rock grain phase (**Figure 9**). At 0.5 PV of MENP injection, NAPL layers with 12.2 µm thickness were adsorbed on the mineral surfaces and covered almost all the grain surfaces. The thinning process started at 1 PV with a thickness reduced to 6.5 µm. After 2 PV of MENP injection, a significant portion of the adsorbed NAPL layers was cleaned up and their average thickness decreased to 2.3 µm. This dynamic solubilization process reached equilibrium after 5 PV of MENP injection when the average layer thickness decreased to a value below the image resolution limit. The ability of MENP to solubilize adsorbed layers resulted in a wettability restoration and its dynamics was consistent with the *in-situ* contact angle distributions in **Figure 5**. This solubilization contributed to 16% of additional NAPL removal at a later stage of nanofluid flooding (2, 5, and 10 PV).

4 CONCLUSIONS

The dynamics of NAPL displacement in porous media was examined using Fond Du Lac carbonate, Permian crude oil, and MENP nanofluid containing microemulsions stabilized by *in-situ* synthesized nanoparticles. After establishing an initial water saturation of 10%, the aged carbonate was subjected to core-flooding experiments under capillary flow regime with various pore volumes of injected MENP and visualized by x-ray microtomography. A systematic analysis of the dynamic IFT, *in-situ* contact angle distribution, emulsified NAPL droplet size, fluid occupancy, saturation profiles, and adsorbed NAPL layer thickness after each flooding was used to understand the dominant displacement mechanisms of NAPL at different stages of nanofluid injection. The main conclusions are summarized below:

1. MENP spontaneously emulsified NAPL into micron-sized droplets (3 μm) and effectively mobilized some of them through the rock during the first pore volume of nanofluid injection. The piston-like mobilization mechanism resulted from a sharp decrease in NAPL/brine IFT (0.5 mN/m) and average in-situ contact angle (88°).
2. With increasing concentration of nanofluid delivered into the rock through advection and diffusion, NAPL droplets became even smaller (2.6 μm) and were able to invade into small pores and alter their wettability. The dynamic solubilization process reached equilibrium after 5 PV of MENP injection, leading to a reduced NAPL layer thickness (0.2 μm), a narrower *in-situ* contact angle distribution (81°), and an additional 16 vol% of NAPL removal.

5 ACKNOWLEDGMENTS

The authors would like to thank Alchemy Sciences Inc., the National Science Foundation (Career Award #1351296), and the European Research Council (ERC-2014-CoG, Project reference: 648375) for financial support. The authors are also grateful to Elizabeth Barsotti of Piri Research Group at the Centre of Innovation for Flow through Porous Media of the University of Wyoming for QEMSCAN imaging and analysis.

6 REFERENCES

(1) Javanbakht, G.; Goual, L. Mobilization and Micellar Solubilization of NAPL Contaminants in Aquifer Rocks. *J. Contam. Hydrol.* **2016**, *185–186*, 61–73. https://doi.org/10.1016/j.jconhyd.2016.01.003.

(2) Javanbakht, G.; Arshadi, M.; Qin, T.; Goual, L. Micro-Scale Displacement of NAPL by Surfactant and Microemulsion in Heterogeneous Porous Media. *Adv. Water Resour.* **2017**, *105*, 173–187. https://doi.org/10.1016/j.advwatres.2017.05.006.

(3) Qin, T.; Javanbakht, G.; Goual, L.; Piri, M.; Towler, B. Microemulsion-Enhanced Displacement of Oil in Porous Media Containing Carbonate Cements. *Colloids Surf. A. Physicochem. Eng. Asp.* **2017**, *530*, 60–71. https://doi.org/10.1016/j.colsurfa.2017.07.017.

(4) Hu, Z.; Nourafkan, E.; Gao, H.; Wen, D. Microemulsions Stabilized by In-Situ Synthesized Nanoparticles for Enhanced Oil Recovery. *Fuel* **2017**, *210*, 272–281. https://doi.org/10.1016/j.fuel.2017.08.004.

(5) Mirchi, V.; Sabti, M. J.; Piri, M.; Goual, L. Microscale Investigation of the Impact of Surfactant Structure on the Residual Trapping in Natural Porous Media. *Ind. Eng. Chem. Res.* **2019**, *58* (22), 9397–9411. https://doi.org/10.1021/acs.iecr.9b00748.

(6) Unsal, E.; Broens, M.; Armstrong, R. T. Pore Scale Dynamics of Microemulsion Formation. *Langmuir* **2016**, *32* (28), 7096–7108. https://doi.org/10.1021/acs.langmuir.6b00821.

(7) Nascimento, D. F. do; Junior, J. R. V.; Paciornik, S.; Carvalho, M. S. Pore Scale Visualization of Drainage in 3D Porous Media by Confocal Microscopy. *Sci. Rep.* **2019**, *9* (1), 1–11. https://doi.org/10.1038/s41598-019-48803-z.

(8) Tagavifar, M.; Xu, K.; Jang, S. H.; Balhoff, M. T.; Pope, G. A. Spontaneous and Flow-Driven Interfacial Phase Change: Dynamics of Microemulsion Formation at the Pore Scale. *Langmuir* **2017**, *33* (45), 13077–13086. https://doi.org/10.1021/acs.langmuir.7b02856.

(9) Alzahid, Y. A.; Mostaghimi, P.; Alqahtani, N. J.; Sun, C.; Lu, X.; Armstrong, R. T. Oil Mobilization and Solubilization in Porous Media by in Situ Emulsification. *J. Colloid Interface Sci.* **2019**, *554*, 554–564. https://doi.org/10.1016/j.jcis.2019.07.009.

(10) Hammond, P. S.; Unsal, E. A Dynamic Pore Network Model for Oil Displacement by Wettability-Altering Surfactant Solution. *Transp. Porous Media* **2012**, *92* (3), 789–817. https://doi.org/10.1007/s11242-011-9933-4.

(11) Reynolds, C. A.; Menke, H.; Andrew, M.; Blunt, M. J.; Krevor, S. Dynamic Fluid Connectivity during Steady-State Multiphase Flow in a Sandstone. *Proc. Natl. Acad. Sci.* **2017**, *114* (31), 8187–8192. https://doi.org/10.1073/pnas.1702834114.

(12) Berg, S.; Ott, H.; Klapp, S. A.; Schwing, A.; Neiteler, R.; Brussee, N.; Makurat, A.; Leu, L.; Enzmann, F.; Schwarz, J.-O.; et al. Real-Time 3D Imaging of Haines Jumps in Porous Media Flow. *Proc. Natl. Acad. Sci.* **2013**, *110* (10), 3755–3759. https://doi.org/10.1073/pnas.1221373110.

(13) Londergan, J.; Yeh, L. *Surfactant-Enhanced Aquifer Remediation (SEAR) Implementation Manual*; INTERA INC AUSTIN TX, 2003.

(14) Chevalier, L. R. Surfactant Dissolution and Mobilization of LNAPL Contaminants in Aquifers. *Environ. Monit. Assess.* **2003**, *84* (1), 19–33. https://doi.org/10.1023/A:1022870626617.

(15) Zhong, L.; Mayer, A. S.; Pope, G. A. The Effects of Surfactant Formulation on Nonequilibrium NAPL Solubilization. *J. Contam. Hydrol.* **2003**, *60* (1), 55–75. https://doi.org/10.1016/S0169-7722(02)00063-3.

(16) Qin, T.; Goual, L.; Piri, M. Synergistic Effects of Surfactant Mixtures on the Displacement of Nonaqueous Phase Liquids in Porous Media. *Colloids Surf. A. Physicochem. Eng. Asp.* **2019**, 123885. https://doi.org/10.1016/j.colsurfa.2019.123885.

(17) Unsal, E.; Rücker, M.; Berg, S.; Bartels, W. B.; Bonnin, A. Imaging of Compositional Gradients during in Situ Emulsification Using X-Ray Micro-Tomography. *J. Colloid Interface Sci.* **2019**, *550*, 159–169. https://doi.org/10.1016/j.jcis.2019.04.068.

(18) Li, M.; Tang, Y. B.; Li, X. F. Dynamic Network Modeling of Displacement and Oil Recovery in Dilute Surfactant Flooding. *Energy Sources Part Recovery Util. Environ. Eff.* **2017**, *39* (9), 926–932. https://doi.org/10.1080/15567036.2016.1276649.

(19) Ezrahi, S.; Aserin, A.; Garti, N. Aggregation Behavior in One-Phase (Winsor IV) Microemulsion Systems. *Handb. Microemulsion Sci. Technol. N. Y. Inf. Inc* **1999**, 185–246.

(20) Bohlen, D. S.; Vinson, P. K.; Davis, H. T.; Scriven, L. E.; Xie, M.; Zhu, X.; Miller, G. W. Generic Patterns in the Microstructure of Midrange Microemulsions. *Organ. Solut. Surfactant Sci. Ser.* **1992**, 145–158.

(21) Karimi, A.; Fakhroueian, Z.; Bahramian, A.; Pour Khiabani, N.; Darabad, J. B.; Azin, R.; Arya, S. Wettability Alteration in Carbonates Using Zirconium Oxide Nanofluids: EOR Implications. *Energy Fuels* **2012**, *26* (2), 1028–1036. https://doi.org/10.1021/ef201475u.

(22) Chevalier, Y.; Bolzinger, M.-A. Emulsions Stabilized with Solid Nanoparticles: Pickering Emulsions. *Colloids Surf. A. Physicochem. Eng. Asp.* **2013**, *439*, 23–34. https://doi.org/10.1016/j.colsurfa.2013.02.054.

(23) Babak, V. G.; Stébé, M.-J. Highly Concentrated Emulsions: Physicochemical Principles of Formulation. *J. Dispers. Sci. Technol.* **2002**, *23* (1–3), 1–22. https://doi.org/10.1080/01932690208984184.

(24) Vrij, A.; Overbeek, J. Th. G. Rupture of Thin Liquid Films Due to Spontaneous Fluctuations in Thickness. *J. Am. Chem. Soc.* **1968**, *90* (12), 3074–3078. https://doi.org/10.1021/ja01014a015.

(25) Worthen, A. J.; Bryant, S. L.; Huh, C.; Johnston, K. P. Carbon Dioxide-in-Water Foams Stabilized with Nanoparticles and Surfactant Acting in Synergy. *AIChE J.* **2013**, *59* (9), 3490–3501. https://doi.org/10.1002/aic.14124.

(26) Jawitz, J. W.; Annable, M. D.; Rao, P. S. C.; Rhue, R. D. Field Implementation of a Winsor Type I Surfactant/Alcohol Mixture for in Situ Solubilization of a Complex LNAPL as a Single-Phase Microemulsion. *Environ. Sci. Technol.* **1998**, *32* (4), 523–530. https://doi.org/10.1021/es970507i.

(27) Penny, G. S.; Zelenev, A.; Lett, N.; Paktinat, J.; O' Neil, B. J. Nano Surfactant System Improves Post Frac Oil and Gas Recovery in Hydrocarbon Rich Gas Reservoirs; Society of Petroleum Engineers, 2012. https://doi.org/10.2118/154308-MS.

(28) Healy, R. N.; Reed, R. L.; Carpenter, C. W. A Laboratory Study of Microemulsion Flooding (Includes Associated Papers 6395 and 6396). *Soc. Pet. Eng. J.* **1975**, *15* (01), 87–103. https://doi.org/10.2118/4752-PA.

(29) Kuang, W.; Saraji, S.; Piri, M. A Systematic Experimental Investigation on the Synergistic Effects of Aqueous Nanofluids on Interfacial Properties and Their Implications for Enhanced Oil Recovery. *Fuel* **2018**, *220*, 849–870. https://doi.org/10.1016/j.fuel.2018.01.102.

(30) Yang, G. C. C.; Chang, Y.-I. Integration of Emulsified Nanoiron Injection with the Electrokinetic Process for Remediation of Trichloroethylene in Saturated Soil. *Sep. Purif. Technol.* **2011**, *79* (2), 278–284. https://doi.org/10.1016/j.seppur.2011.03.004.

(31) Goual, L.; Qin, T.; Javanbakht, G.; Piri, M. Microemulsions and Uses Thereof to Displace Oil in Heterogeneous Porous Media, Provisional Patent 15/367,478, University of Wyoming, 2016.

(32) Jiang, R.; Kunz, H. R.; Fenton, J. M. Composite Silica/Nafion® Membranes Prepared by Tetraethylorthosilicate Sol–Gel Reaction and Solution Casting for Direct Methanol Fuel Cells. *J. Membr. Sci.* **2006**, *272* (1), 116–124. https://doi.org/10.1016/j.memsci.2005.07.026.

(33) Lindberg, R.; Sjöblom, J.; Sundholm, G. Preparation of Silica Particles Utilizing the Sol-Gel and the Emulsion-Gel Processes. *Colloids Surf. A. Physicochem. Eng. Asp.* **1995**, *99* (1), 79–88. https://doi.org/10.1016/0927-7757(95)03117-V.

(34) Rao, K. S.; El-Hami, K.; Kodaki, T.; Matsushige, K.; Makino, K. A Novel Method for Synthesis of Silica Nanoparticles. *J. Colloid Interface Sci.* **2005**, *289* (1), 125–131. https://doi.org/10.1016/j.jcis.2005.02.019.

(35) Stöber, W.; Fink, A.; Bohn, E. Controlled Growth of Monodisperse Silica Spheres in the Micron Size Range. *J. Colloid Interface Sci.* **1968**, *26* (1), 62–69. https://doi.org/10.1016/0021-9797(68)90272-5.

(36) Saraji, S.; Goual, L.; Piri, M.; Plancher, H. Wettability of Supercritical Carbon Dioxide/Water/Quartz Systems: Simultaneous Measurement of Contact Angle and Interfacial Tension at Reservoir Conditions. *Langmuir* **2013**, *29* (23), 6856–6866.

(37) Li, Z.; Yu, L.; Trzasko, J. D.; Lake, D. S.; Blezek, D. J.; Fletcher, J. G.; McCollough, C. H.; Manduca, A. Adaptive Nonlocal Means Filtering Based on Local Noise Level for CT Denoising. *Med. Phys.* **2014**, *41* (1), 011908. https://doi.org/10.1118/1.4851635.

(38) Wildenschild, D.; Sheppard, A. P. X-Ray Imaging and Analysis Techniques for Quantifying Pore-Scale Structure and Processes in Subsurface Porous Medium Systems. *Adv. Water Resour.* **2013**, *51*, 217–246. https://doi.org/10.1016/j.advwatres.2012.07.018.

(39) Zana, R. Aqueous Surfactant-Alcohol Systems: A Review. *Adv. Colloid Interface Sci.* **1995**, *57*, 1–64. https://doi.org/10.1016/0001-8686(95)00235-I.

(40) Moghadam, T.F.; Azizian, S. Effect of ZnO Nanoparticle and Hexadecyltrimethylammonium Bromide on the Dynamic and Equilibrium Oil–Water Interfacial Tension. *J. Phys. Chem. B* **2014**, *118* (6), 1527–1534. https://doi.org/10.1021/jp4106986.

(41) Mirchi, V.; Saraji, S.; Akbarabadi, M.; Goual, L.; Piri, M. A Systematic Study on the Impact of Surfactant Chain Length on Dynamic Interfacial Properties in Porous Media: Implications for Enhanced Oil Recovery. *Ind. Eng. Chem. Res.* **2017**, *56* (46), 13677–13695. https://doi.org/10.1021/acs.iecr.7b02623.

(42) Hammond, P. S.; Unsal, E. Forced and Spontaneous Imbibition of Surfactant Solution into an Oil-Wet Capillary: The Effects of Surfactant Diffusion Ahead of the Advancing Meniscus. *Langmuir ACS J. Surf. Colloids* **2010**, *26* (9), 6206–6221. https://doi.org/10.1021/la903924m.

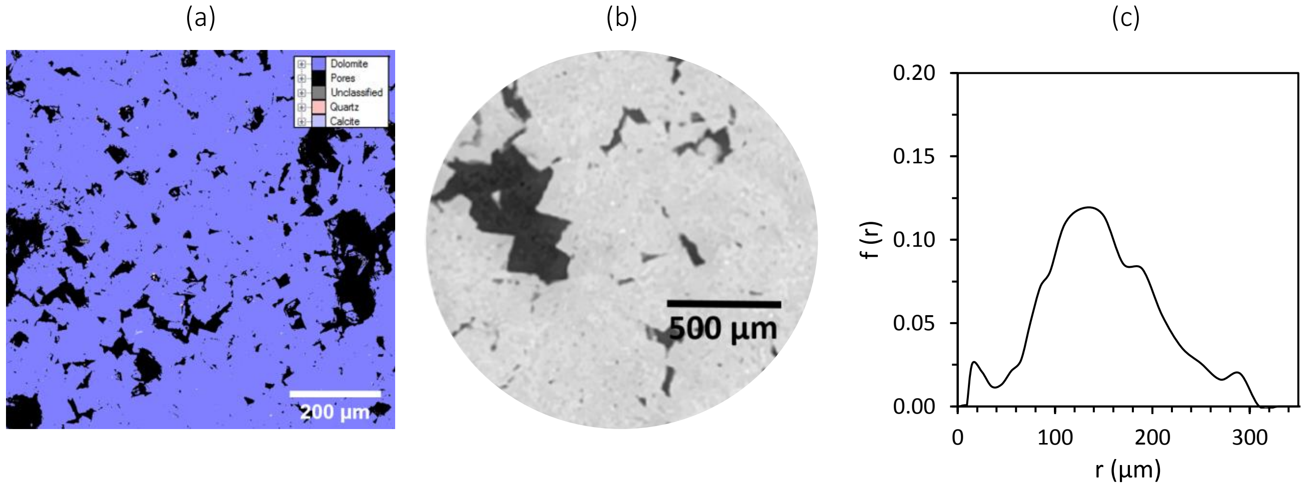

Figure 1. (a) Mineralogy map, (b) x-ray microtomographic image, and (c) pore size distribution of Fond Du Lac carbonate.

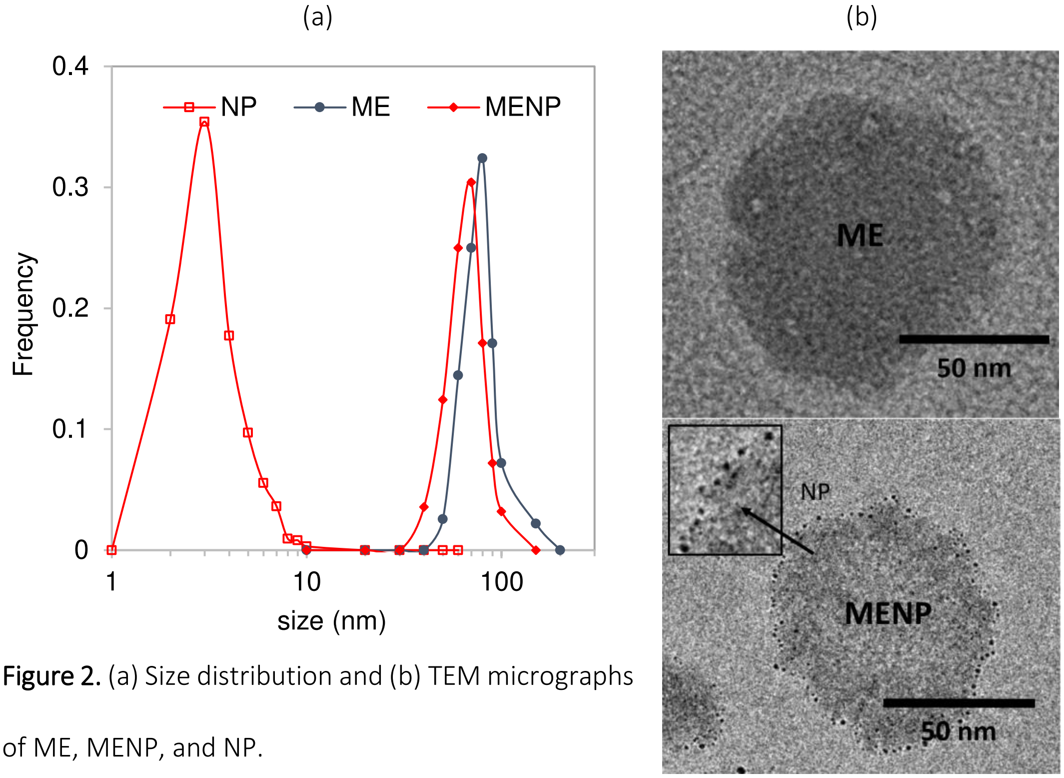

Figure 2. (a) Size distribution and (b) TEM micrographs of ME, MENP, and NP.

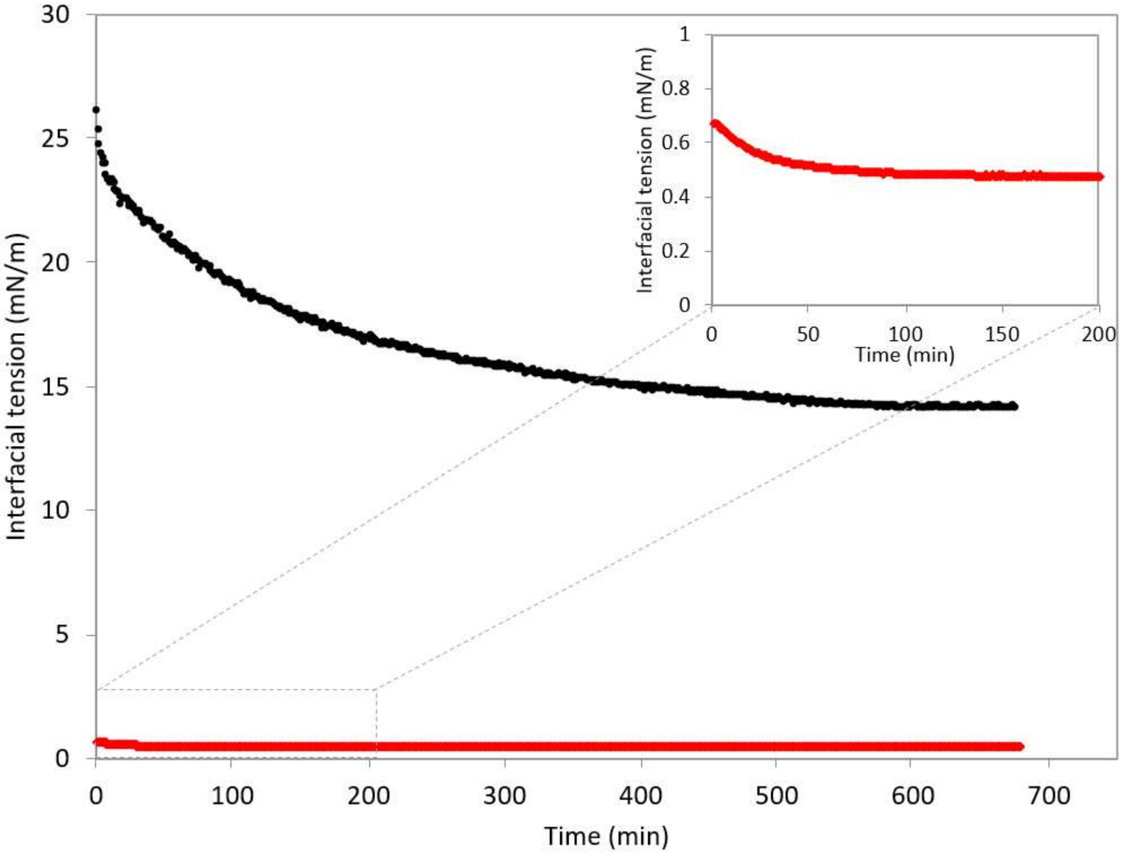

Figure 3. The dynamic interfacial tension between NAPL and brine (with and without MENP) at 60° and 200 psi.

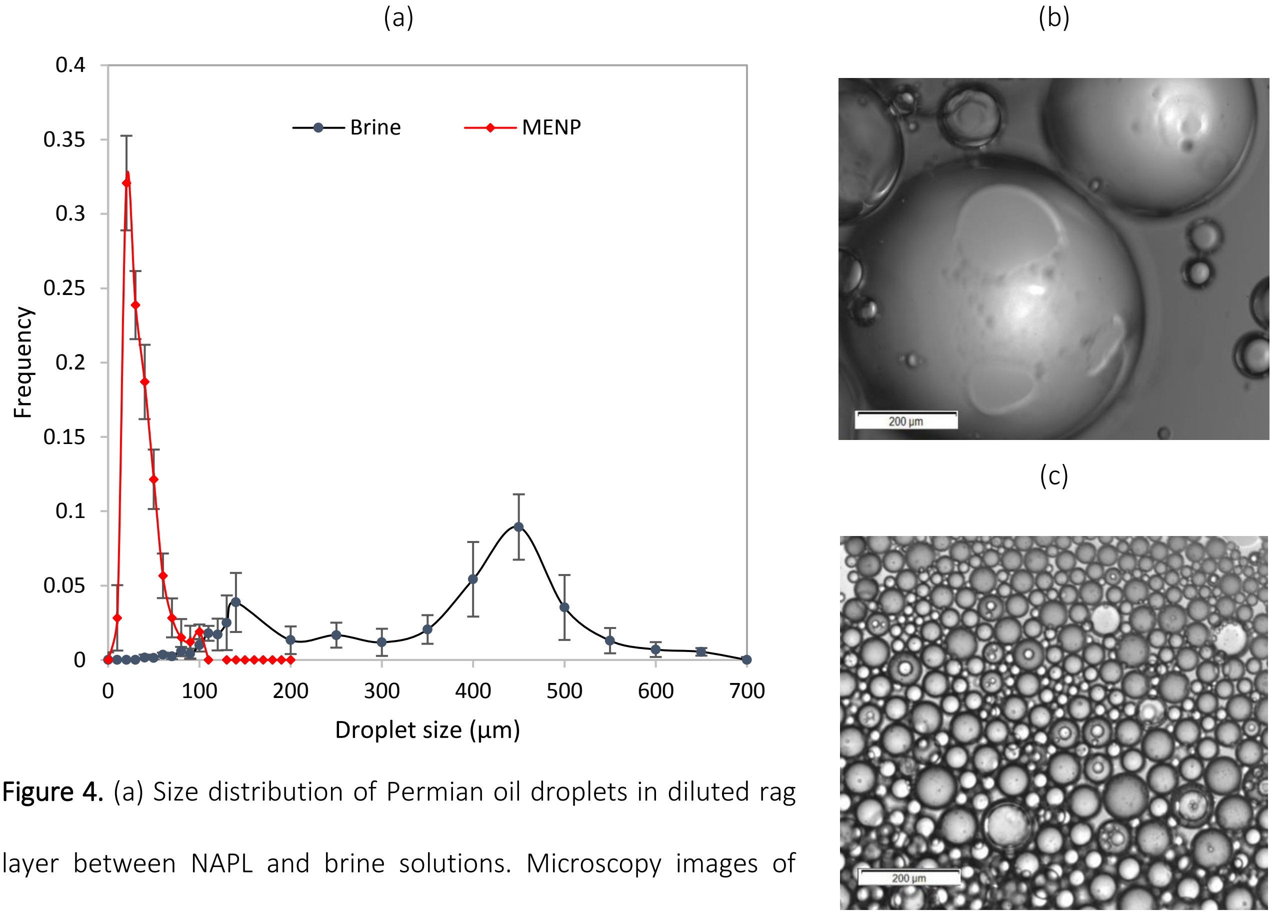

Figure 4. (a) Size distribution of Permian oil droplets in diluted rag layer between NAPL and brine solutions. Microscopy images of these droplets in (b) brine and (c) MENP.

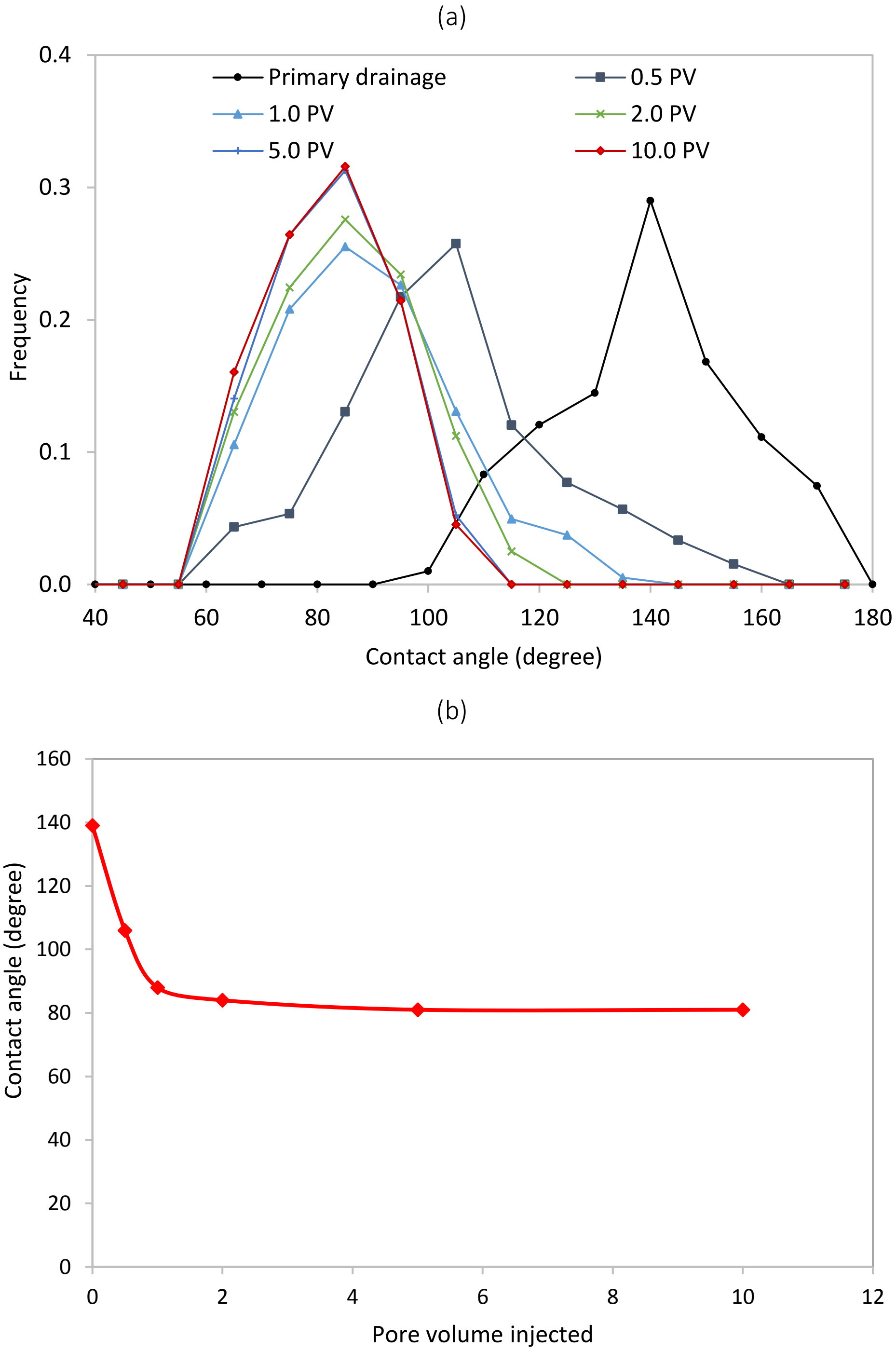

Figure 5. (a) In-situ contact angle distributions, and (b) average contact angles of NAPL droplets after various pore volumes of MENP injection.

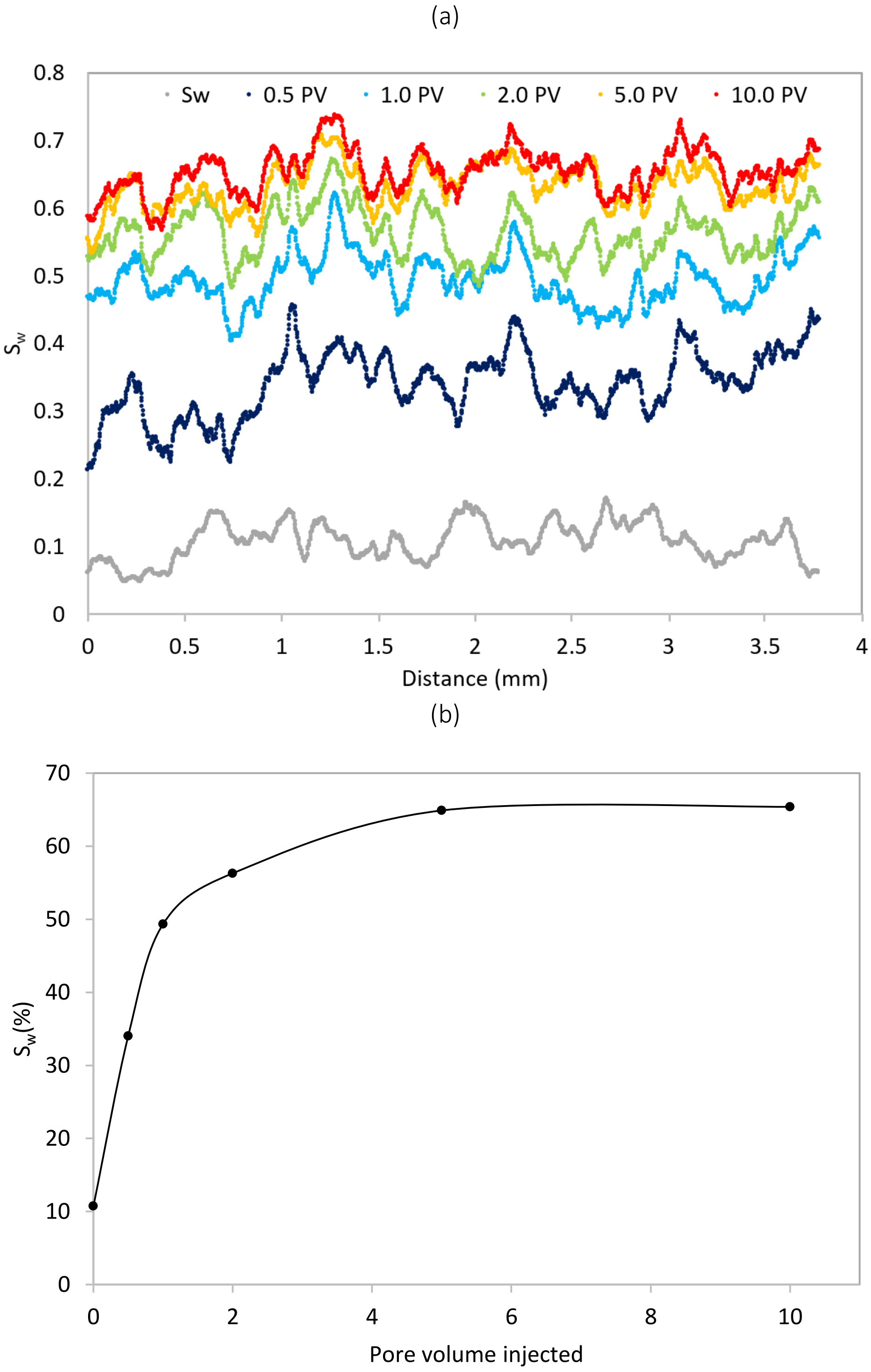

Figure 6. (a) Saturation profile at the end of MENP flooding with various injection pore volumes, and (b) effect of injection pore volume on water saturation in Fond Du Lac carbonate.

(a) Primary Drainage (b) 0.5 PV (c) 1.0 PV

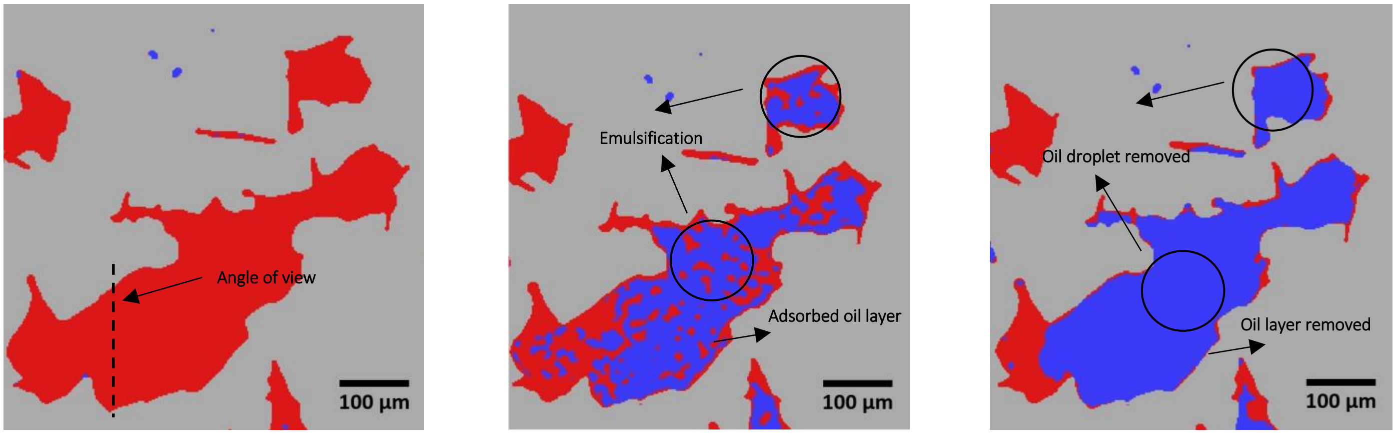

(d) 2.0 PV (e) 5.0 PV (f) 10.0 PV

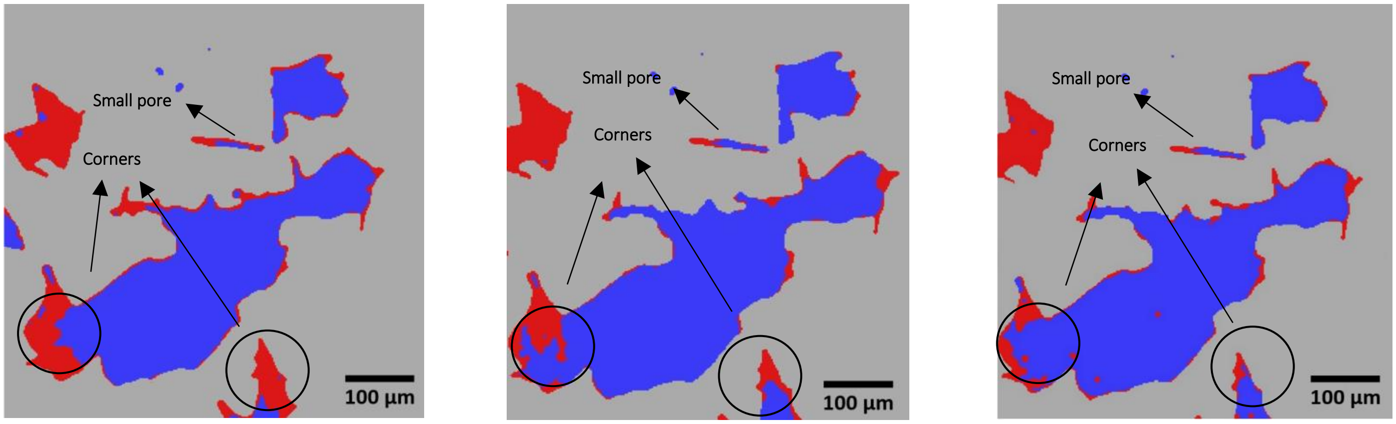

Figure 7. 2D visualization of the pores after (a) primary drainage and injection of (b) 0.5 PV, (c) 1.0 PV, (d) 2.0 PV, (e) 5.0 PV, (f) 10.0 PV of MENP.

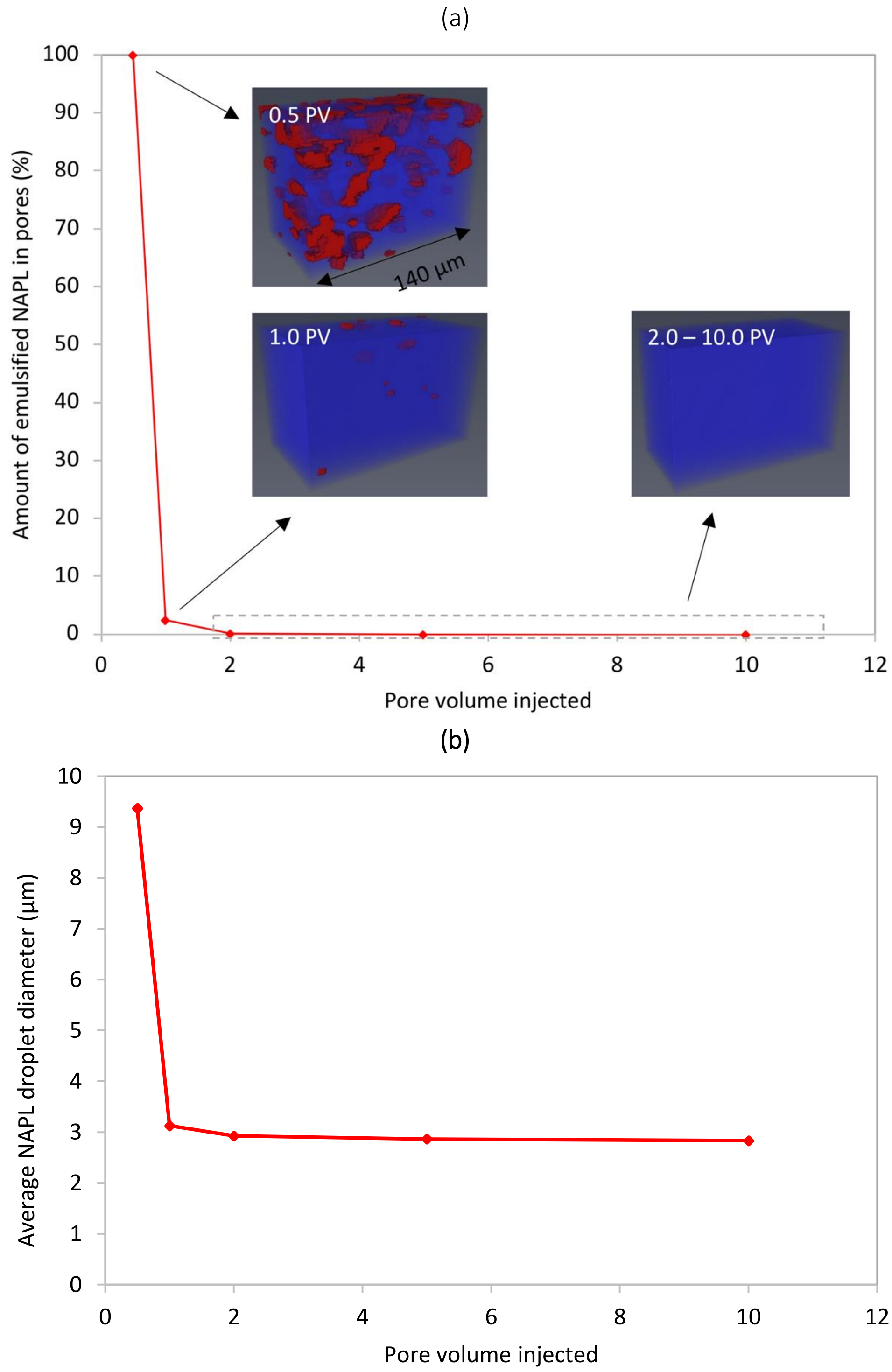

Figure 8. (a) Amount and b) average diameter of emulsified NAPL droplets in pores after various pore volumes of MENP injection.

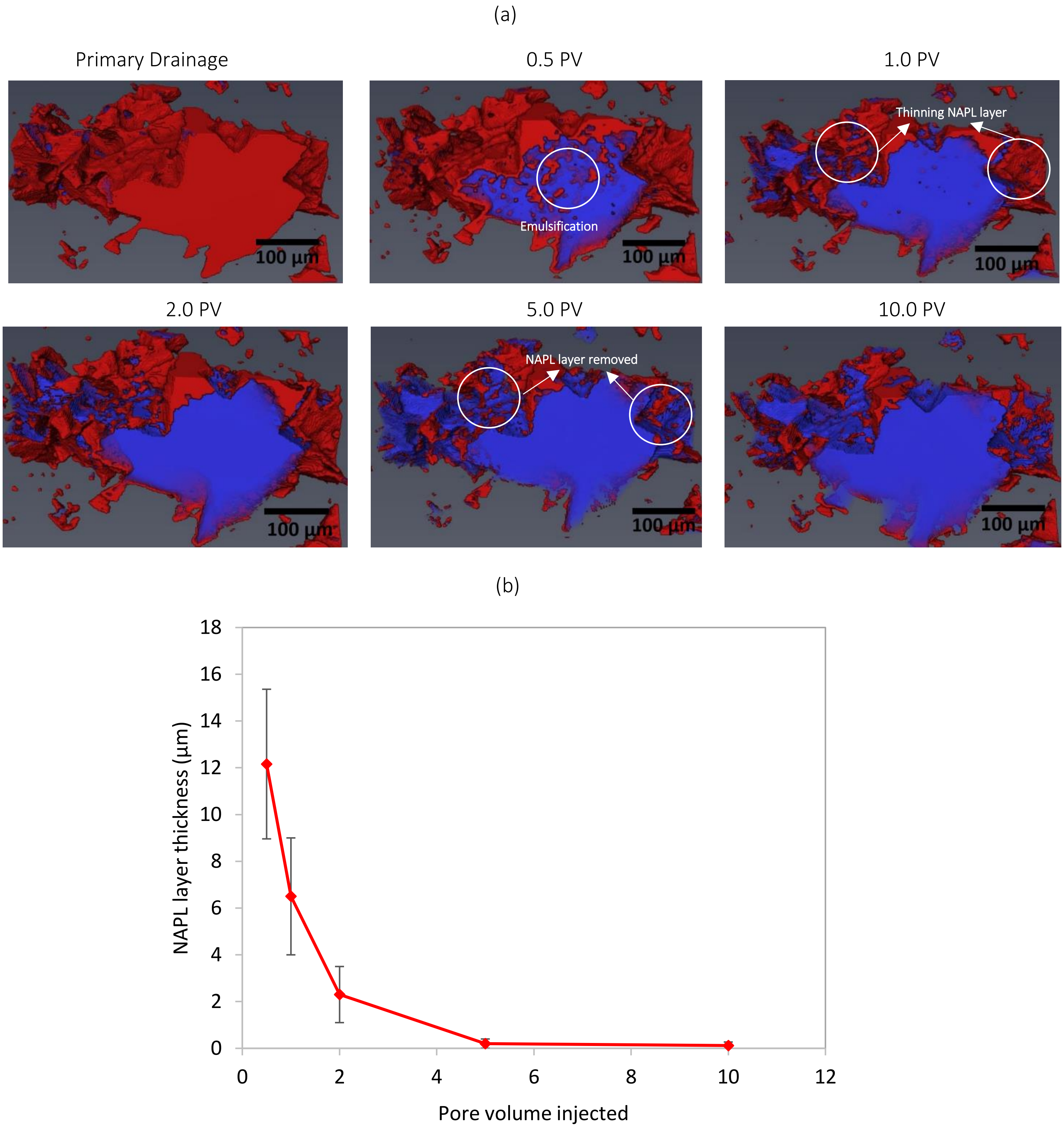

Figure 9. (a) 3D visualization of the pores and (b) variation of adsorbed NAPL layer thickness after various pore volumes of MENP injection.